

ORIGINAL RESEARCH ARTICLE

Analysis of water vapor adsorption in soils by means of a lysimeter and numerical modeling

Maarten W. Saaltink^{1,2}  | Claus Kohfahl³ | Lidia Molano-Leno³

¹Dep. of Civil and Environmental Engineering, Univ. Politècnica de Catalunya (UPC), Jordi Girona 1–3, 08034 Barcelona, Spain

²Associated Unit: Hydrogeology Group (UPC-CSIC), Barcelona, Spain

³Instituto Geológico y Minero de España, Plaza de España, 41013 Seville, Spain

*Correspondence

Maarten Saaltink, Dep. of Civil and Environmental Engineering, Univ. Politècnica de Catalunya (UPC), Jordi Girona 1–3, 08034 Barcelona, Spain.
Email: maarten.saaltink@upc.edu

Funding information

Ministry of Economy, Industry and Competitiveness of Spain, Grant/Award Number: PEJ-2014-A-68763; European Research Funds, Grant/Award Number: IGME13-IE-2113; Ministerio de Ciencia e Innovación, Grant/Award Number: CGL2016-77473-C3-1-R

Abstract

Daily temperature oscillations can cause adsorption (and desorption) of atmospheric water vapor by soils. The resulting daily fluctuations in the amount of liquid water in the soil can be measured by high-precision weighing lysimeters. We analyzed the data of a lysimeter in a sandy dune sediment in southern Spain using Codebright, a thermohydraulic numerical model for unsaturated flow that takes into account water, vapor, and heat transport in the soil, as well as soil–atmosphere interactions such as precipitation, evaporation, and solar radiation. The analysis shows that daily temperature oscillations, psychrometrics, and soil water retention can explain the fluctuations of the amount of liquid water in the soil. The retention curve, especially its driest part, is essential for the existence of these fluctuations. The fluctuations could not be reproduced by a model using the van Genuchten retention curve with a constant residual saturation. On the other hand, satisfactory results could be obtained by models using retention curves that at their driest part still show a change of saturation with suction. Moreover, the models suggest within the top few decimeters of the soil a pattern of alternating bands of condensation and evaporation, which follows the daily temperature oscillations that fade out deeper in the soil.

1 | INTRODUCTION

Non-rainfall water depositions, such as fog deposition, dew, and water vapor adsorption, are important hydrological processes, especially in arid and semiarid regions (Agam & Berliner, 2006; Uclés, Villagarcía, Cantón, Lázaro, & Domingo, 2015; Verhoef, Díaz-Espejo, Knight, Villagarcía, & Fernández, 2006). Agam and Berliner (2006) make a clear distinction between dew and water vapor adsorption. The difference can be explained best by means of a psychrometric chart (Figure 1). Dew formation takes place on flat surfaces,

which requires air to be almost or fully saturated in water vapor (i.e., relative humidity $[H_r] = 1$). Water vapor adsorption refers to the influx of water vapor from the atmosphere into a soil followed by condensation. It involves vapor diffusion and water retention, which at the pore scale is caused not only by mechanic adsorption of water at the surfaces of soil grains but also by capillary and, sometimes, osmotic forces. At the macroscopic scale, this is usually expressed through a retention curve that relates the (liquid) volumetric water content of a soil (VWC) to the water potential, which is equivalent to suction ($p_g - p_1$, see Table 1 for variable definitions). Thus, at this macroscopic scale it is better to use the term absorption rather than adsorption. Nevertheless, in this paper we will use adsorption, because it is the most widely used

Abbreviations: AWAT, adaptive window and adaptive threshold; VWC, volumetric water content.

This is an open access article under the terms of the Creative Commons Attribution License, which permits use, distribution and reproduction in any medium, provided the original work is properly cited.

© 2020 The Authors. *Vadose Zone Journal* published by Wiley Periodicals, Inc. on behalf of Soil Science Society of America

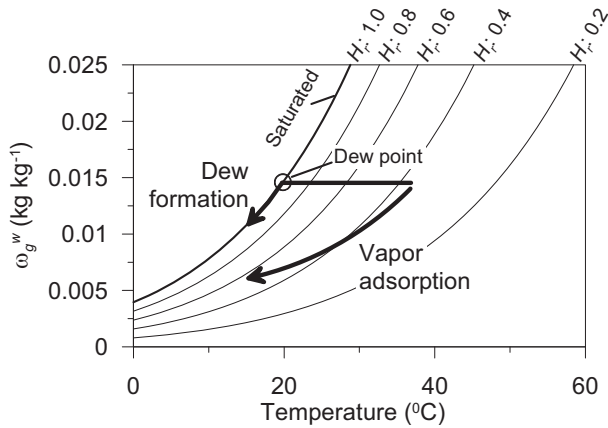


FIGURE 1 Dew formation and water vapor adsorption in a psychrometric chart, developed by Carrier (1911), who also invented the air conditioner. Air is cooled in a closed system. In a system with only flat surfaces, dew will form after the air becomes saturated in water vapor at the dew point. Soils can retain liquid water at positive suction ($p_g - p_l$) or relative humidities (H_r) lower than 1 and, hence, permit vapor condensation at such lower relative humidities. The y axis shows specific humidity (ω_g^w)

term in the literature. Water potential or suction depends on relative humidity (H_r), which in turn is affected by temperature, as illustrated in Figure 1. Hence, heat processes, such as heat conduction within the soil, solar radiation, and latent and sensible heat fluxes at the soil surface, also play an important role in vapor adsorption. In fact, vapor adsorption only takes place during certain hours of the day (Agam & Berliner, 2004), which suggests an essential effect of the daily cycle of temperature and solar radiation. Dew forms mainly on plants and stones, whereas water vapor adsorption is more important for soils and lichens (Uclés et al., 2015). Therefore, dew deposition on a bare soil is probably a rare phenomenon (Agam & Berliner, 2004).

There are numerous experimental studies on dew (see, for instance, Tomaszewicz, Abou Najm, Beysens, Alameddine, and El-Fadel [2015] for a review). However, in our study, we focus on water vapor adsorption in bare soils, and less is published on this subject. Agam and Berliner (2004) measured values for water vapor adsorption of $0.3 \text{ kg m}^{-2} \text{ d}^{-1}$ during 9 d in a coastal desert (Negev) using a microlysimeter and gravimetric hourly measurements of 0.1 m topsoil. Kosmas et al. (2001) measured values of $0.5 \text{ kg m}^{-2} \text{ d}^{-1}$ during the dry period with a weighing lysimeter of 0.4-m depth and a surface of 0.6 m^2 filled with 200 kg of disturbed soil. Verhoef et al. (2006) measured water vapor adsorption during 8 d beside irrigated olive trees in southern Spain using mini weighing lysimeters of 0.25-m depth and obtained up to $0.7 \text{ kg m}^{-2} \text{ d}^{-1}$. Uclés et al. (2015) registered values of up to $0.2 \text{ kg m}^{-2} \text{ d}^{-1}$ using microlysimeters with 0.09-m depth, also for Mediterranean climates. Note that these are

Core Ideas

- Experimental data provide information about vapor flow in dry dune sediments.
- A numerical model could reproduce experimental data of vapor flow on an hourly scale.
- Daily temperature oscillations cause alternating inward and outward vapor flow.
- Calibration reveals critical importance of the dry part of the retention curve.
- Models suggest dominance of vapor flow in the first few decimeters of the soil.

fairly high values in comparison with rainfall and evaporation, and also that they do not differ much from each other.

To quantify or measure water vapor adsorption, the studies mentioned above used gravimetric data of microlysimeters or small weighing lysimeters without lower boundary control. The total mass of water adsorbed in the lysimeter can be deduced from the weight of the lysimeter. However, its natural distribution is more difficult to obtain, and especially small lysimeters and microlysimeters with disturbed soil samples may alter significantly the thermal regime due to the larger influence of their different material properties compared with soil. Furthermore, the no-flow boundary condition imposed by the impermeable (micro-)lysimeter base at a shallow surface may lead to artificial accumulation of water and vapor and therefore requires an experimental setup considering a larger depth and a control to maintain natural humidity conditions at the lysimeter base. Whereas lysimeter weights only give the water vapor adsorption in the whole lysimeter, sensors give more information on its distribution. Concerning the existing measurement systems, the last generation of weighing lysimeters are powerful tools to quantify water balance components with a high precision ($<0.1 \text{ kg m}^{-2}$) and a high temporal resolution (1 min) integrating measurements over larger surface areas and depths (Hannes et al., 2015). State-of-the-art lysimeters are equipped with sensor arrays that measure soil parameters inside and outside of the lysimeter container to monitor and control boundary conditions, similar to that of the undisturbed soil environment (Pütz, Fank, & Fury, 2018, among others). Therefore, larger precision lysimeters with a lower boundary control significantly improve the available dataset representing natural vapor flow processes. To our knowledge, no study has been published presenting modeling results using data of precision lysimeters with lower boundary control in dune sediments.

Nonetheless, for a better understanding of the processes and mechanisms effecting water vapor adsorption and their

TABLE 1 List of variables

Variable	Definition
c_g	Specific heat of gas ($\sim 1 \times 10^3 \text{ J kg}^{-1} \text{ K}^{-1}$)
$D_{\text{dif},\alpha}^i$	Diffusion coefficient of component i in phase α ($\text{m}^2 \text{ s}^{-1}$)
$D_{\text{dis},\alpha}^i$	Dispersion coefficient of component i in phase α ($\text{m}^2 \text{ s}^{-1}$)
D_0	Parameter for vapor diffusion coefficient ($\text{m}^2 \text{ s}^{-1} \text{ K}^{-n} \text{ Pa}$)
E	Turbulent vapor flux at the soil surface ($\text{kg m}^{-2} \text{ s}^{-1}$)
e_α^i	Internal energy of component i in phase α (J kg^{-1})
f^i	External source/sink of component i ($\text{kg m}^{-3} \text{ s}^{-1}$)
g	Gravitational acceleration ($= -9.81 \text{ m s}^{-2}$)
H	Sensible heat flux ($\text{J m}^{-2} \text{ s}^{-1}$)
H_r	Relative humidity
j_α^i	Mass flux of component i in phase α ($\text{kg m}^{-2} \text{ s}^{-1}$)
$j_{\text{dif},g}^w$	Vapor diffusion in soil ($\text{kg m}^{-2} \text{ s}^{-1}$)
k	Von Karman's constant ($= 0.4$)
K_{int}	Intrinsic permeability (m^2)
$k_{r,\alpha}$	Relative permeability of phase α ($-$)
m	Van Genuchten shape parameter ($-$)
n	Parameter for vapor diffusion coefficient ($-$)
M^w	Molecular weight of water ($= 0.018 \text{ kg mol}^{-1}$)
P	Precipitation ($\text{kg m}^{-2} \text{ s}^{-1}$)
p_α	Pressure of phase α (Pa)
p_e	Air-entry pressure (Pa)
p_{dry}	Parameter for the Rossi and Nimmo retention curve (Pa)
q_α	Darcy flux of phase α (m s^{-1})
r_a	Aerodynamic resistance (s m^{-1})
R_g	Gas constant ($= 8.314 \text{ J mol}^{-1} \text{ K}^{-1}$)
R_n	Net radiation ($\text{J m}^{-2} \text{ s}^{-1}$)
S_α	Saturation of phase α ($\text{m}^3 \text{ m}^{-3}$)
$S_{\alpha,e}$	Effective saturation of phase α ($\text{m}^3 \text{ m}^{-3}$)
$S_{\alpha,r}$	Residual saturation of phase α ($\text{m}^3 \text{ m}^{-3}$)
$S_{\alpha,s}$	Maximum saturation of phase α ($\text{m}^3 \text{ m}^{-3}$)
T	Temperature ($^\circ\text{C}$)
v	Wind velocity (m s^{-1})
z_a	Height at which meteorological data are measured (m)
z_0	Roughness length (m)
α	Parameter for the Rossi and Nimmo retention curve
λ	Thermal conductivity ($\text{J } ^\circ\text{C}^{-1} \text{ m}^{-1} \text{ s}^{-1}$)
λ_{dry}	Thermal conductivity of dry soil ($\text{J } ^\circ\text{C}^{-1} \text{ m}^{-1} \text{ s}^{-1}$)
λ_{sat}	Thermal conductivity of saturated soil ($\text{J } ^\circ\text{C}^{-1} \text{ m}^{-1} \text{ s}^{-1}$)
μ_α	Viscosity of phase α (Pa s)
ρ_α	Density of phase α (kg m^{-3})
σ	Temperature dependent surface tension of the gas–liquid interface (N m^{-1})
σ_{20}	Surface tension of the gas–liquid interface at $20 \text{ } ^\circ\text{C}$ ($= 0.072 \text{ N m}^{-1}$)
τ	Factor for tortuosity and enhancement of vapor diffusion ($-$)
ϕ	Porosity ($\text{m}^3 \text{ m}^{-3}$)
ω_α^i	Mass fraction of component i in phase α (kg^{-1})

(Continues)

TABLE 1 (Continued)

Variable	Definition
$\omega_{g,sat}^w$	Saturated specific humidity (kg^{-1})
Superscripts for component i	
a	Air
w	Water
Subscripts for phase α	
g	Gas
l	Liquid
s	Solid

Note. Upward fluxes and fluxes into the soil are always positive. Downward fluxes and fluxes out of the soil are always negative. Water fluxes are expressed in $\text{kg m}^{-2} \text{s}^{-1}$, which is equivalent to mm s^{-1} of liquid water with a density of $1,000 \text{ kg m}^{-3}$.

distributions, the improved experimental design and dataset requires model-based numerical evaluation. These models should simulate on a macroscopic scale the transport of water (both as liquid and as vapor) and heat in unsaturated soils together with meteorological phenomena, such as rainfall, evaporation, solar radiation, and heat exchange with the atmosphere. Evaporation, or more precisely vapor flux, across the soil surface and sensible heat flux are usually treated by an aerodynamic resistance that accounts for the turbulent mixing of heat and vapor in the air above the soil surface (van Bavel & Hillel, 1976). Vapor diffusion within the soil is driven by gradients of both temperature and VWC (Philip & de Vries, 1957). This was used by Milly (1982) for the development of early numerical models that simulate coupled heat and water transport in unsaturated soils. This modeling approach has been maintained with some minor changes. For instance, Grifoll (2013) concluded that it is important to also consider vapor dispersion due to Stefan flow (i.e., flow induced by evaporation located at some distance below the soil surface). As water vapor adsorption is a diurnal phenomenon only taking place at certain hours of the day, it is important to consider the effects of daily oscillations of temperature and solar radiation on water and heat flow in soils. These effects have been analyzed by many models (Grifoll, Gastó, & Cohen, 2005; Jiang, Zhao, & Zhai, 2016; Saito, Šimůnek, & Mohanty, 2006; Zeng et al., 2009), also in combination with weighing lysimeters (Dijkema et al., 2018). However, numerical models have not been used for studying specifically water vapor adsorption.

The objective of this paper is to analyze the complex relation between heat transport, water flow, vapor diffusion, and water retention and to see to what extent it can explain the observed phenomenon of water vapor adsorption. We used data from a precision weighing meteo-lysimeter experiment in sandy dune sediments in southern Spain (Kohfahl et al., 2019). These data are used for a numerical model that aims to simulate all relevant thermohydraulic processes. The innovative aspect of this work is the specific application

of a numerical model to water vapor adsorption based on a novel, high-precision data set of soil water balance in dune sediments.

2 | LYSIMETER AND LABORATORY EXPERIMENTS

2.1 | Weighing lysimeter characteristics

A high precision meteo-lysimeter (Meter Group), composed of a hydrolysimeter and a meteorological station, was installed in September 2015 on a flat roof of a stabilized dune in the Natural Reserve of the Doñana National Park Southwest Spain ($37^{\circ} 1' 19.49'' \text{ N}$; $6^{\circ} 33' 17.77'' \text{ W}$).

The location of the lysimeter is characterized by sandy soil and an unsaturated zone of $>8 \text{ m}$ above the phreatic groundwater level. Analysis of the aeolian dune sand samples showed a similar grain size distribution of medium sands with $\sim 30\%$ fine-grained material below 0.2 mm . The homogeneous composition is in agreement with the macroscopic character of the soil identified in the wall of an open pit showing homogeneous dune sands without any kind of visually detectable stratification.

To maintain undisturbed soil conditions, the lysimeter cylinder was inserted vertically into the soil without vegetation. The hydrolysimeter has a soil surface area of 1 m^2 , which was always maintained free of vegetation, a height of 1.5 m , a weight resolution of 10 g , and an error of 100 g . The lower boundary control was performed by two tensiometers (UMS T8, Meter Group, with measurement ranges between -85 and 0 kPa), installed at 1.4-m depth in and outside the lysimeter in undisturbed soil. A bidirectional peristaltic pump maintained the same soil water pressure in the lysimeter as measured by the tensiometer outside the lysimeter. Drainage volume was measured directly by monitoring weight increments of the drainage vessel installed in the maintenance well beside the lysimeter. Intrinsic noise of the lysimeter weight

TABLE 2 Main parameters used for the models

Parameter	Symbol	Value
Van Genuchten retention curve	p_0	34 hPa
	$S_{1,s}$	1.0
	m	0.76
	$S_{1,r}$	0.15
Rossi and Nimmo retention curve	p_0	34 hPa
	p_{dry}	1×10^7 hPa
	m	0.76
	α	0.1
	$S_{1,s}$	1.0
	S_0	0.15
Double porosity retention curve	$p_{0,1}$	34 hPa
	$p_{0,2}$	5×10^5 hPa
	m_1	0.76
	m_2	0.5
	f_1	0.85
	f_2	0.15
Porosity	ϕ	0.37
Solid density	ρ_s	$2,670 \text{ kg m}^{-3}$
Permeability	\mathbf{K}_{int}	$1.0 \times 10^{-11} \text{ m}^2$
	m	0.76
Vapor diffusion	D_0	$5.6 \times 10^{-6} \text{ m}^2 \text{ s}^{-1} \text{ K}^{-2.3} \text{ Pa}$
	n	2.3
	τ	6.0
Thermal conductivity	λ_g	$0.025 \text{ J K}^{-1} \text{ m}^{-1} \text{ s}^{-1}$
	λ_l	$0.60 \text{ J K}^{-1} \text{ m}^{-1} \text{ s}^{-1}$
	λ_s	$2.0 \text{ J K}^{-1} \text{ m}^{-1} \text{ s}^{-1}$
Atmospheric parameters	z_a	2.0 m
	z_0	0.01 m

Note. τ , λ , and z_0 are obtained from calibration. See Table 1 for parameter definitions.

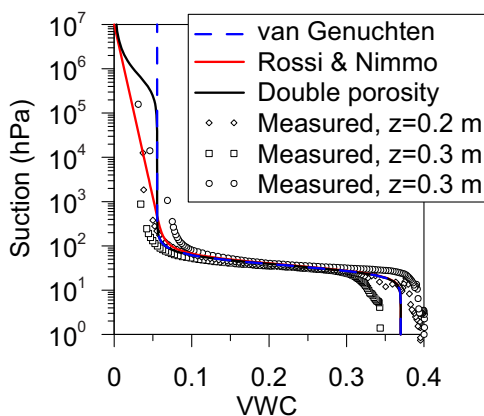


FIGURE 2 Retention curves used by the models together with data from laboratory experiments. The experimental data are for three samples, one taken from a depth (z) of 0.2 m, and two others from a depth of 0.3 m. The x axis shows the volumetric water content (VWC)

and the drainage vessel weight data was reduced by smoothing using the adaptive window and adaptive threshold (AWAT) filter (Peters, Nehls, Schonsky, & Wessolek, 2014), which has been applied successful in other lysimeter studies (Hoffmann, Schwartengraber, Wessolek, & Peters, 2016). Weight measurements were carried out at one minute and all other data at 10-min intervals. For a more detailed description of the lysimeter, we refer to Kohfahl et al. (2019).

Precipitation was measured by an external tipping bucket rain gauge, with a surface of 400 cm^2 , according to World Meteorological Organization standard, and a resolution of 0.1 mm (RG2013-0.1, UMS). Moreover, other meteorological data were measured with 10-min time intervals, including temperature, relative humidity, and wind velocity at 2-m height and net radiation at the soil surface.

Following Schrader, Durner, Fank, Gebler, and Pütz (2013) and Kohfahl et al. (2019), we calculated inward vapor

flux across the soil surface or water vapor adsorption, E_{in} , straightforwardly through a water balance from measured rainfall by the pluviometer (P) and the weights of the lysimeter (W_{lys}), and drainage vessel (W_{drain}):

$$\begin{cases} P + E_{in} = \frac{\Delta W_{lys}}{\Delta t} + \frac{\Delta W_{drain}}{\Delta t}, & \text{if } \frac{\Delta W_{lys}}{\Delta t} + \frac{\Delta W_{drain}}{\Delta t} > 0 \\ P + E_{in} = 0, & \text{if } \frac{\Delta W_{lys}}{\Delta t} + \frac{\Delta W_{drain}}{\Delta t} \leq 0 \end{cases} \quad (1)$$

Note that the weight of the solid in the lysimeter is assumed to be constant, so that the change of total weight of the lysimeter equals that of the water. Equation 1 works well when there is no precipitation. During rainfall events, it may be inaccurate due to differences in measured rainfall by the pluviometer compared with upper boundary flow weight changes registered by the lysimeter ($\Delta W_{lys}/\Delta t$). Nonetheless, we assume this error is not significant, because vapor adsorption is negligible during rainfall.

2.2 | Soil moisture sensors and soil water retention curves

Five CS650 (Campbell Scientific) soil moisture sensors were installed horizontally in undisturbed soil in the wall of the open pit next to the lysimeter at three different depths ranging from 0.3 to 1.2 m below surface. The accuracy of the VWC measurements ($\pm 3\%$) was confirmed gravimetrically by undisturbed soil sampling using stainless steel rings of 0.053- and 0.103-m diameter (Kohfahl et al., 2019). The measured data are available from the supplemental material.

Duplicate samples for laboratory analysis were taken with 250-cm³ sampling rings at 0.2-, 0.3-, and 0.6-m depth for soil water retention curves and analyzed at LAB-FERRER (Decagon Devices) depth using the hydraulic properties analyzer (METER GROUP). Four soil samples were taken at depths 0.3 and 0.6 m for soil moisture sensor calibration. To check soil heterogeneity, doubled samples were taken from the open pit during lysimeter construction, every 0.5 m down to a depth of 3 m, and stored in plastic bags for subsequent analysis of grain size distribution by fractionated sieving with water according to DIN 66165-1 and -2 (1987). All samples were taken outside the lysimeter and therefore did not damage undisturbed soil conditions in the lysimeter. Infiltration tests for saturated hydraulic conductivity were performed using 100-mm-diam. polyvinyl chloride (PVC) rings with a height of 220-mm infiltration according to Hatt and Le Coustumer (2008).

3 | NUMERICAL MODEL

The lysimeter experiment is simulated by using CODE-BRIGHT, a finite element code for modeling multiphase flow

and heat transport (Olivella, Gens, Carrera, & Alonso, 1996). The lysimeter is represented by a vertical one-dimensional finite element grid of 1.4-m length, divided into 140 elements of 0.01 m. The domain is homogeneous, representing the homogeneous dune sand. The model calculations start on 25 Nov. 2015 and end on 4 Oct. 2017, which is the period with available meteorological data. The code solves balance equations for water (both vapor and liquid), air, and heat, using standard mathematical equations as explained in the appendix. Below we describe the constitutive laws, parameters, and boundary conditions used by the models.

3.1 | Constitutive laws and parameters

Constitutive laws are used to write variables used in Equations A1–A3 as functions of the state variables (p_l , p_g , and T). Only the most relevant are described and discussed below. Table 2 gives the most important parameter values. Moreover, densities (ρ), viscosities (μ) of gas and liquid, and surface tension (σ) of the gas–liquid interface all depend on temperature through standard functions. For more details, we refer to Olivella, Carrera, Gens, and Alonso (1994) and Olivella et al. (1996).

Solid density, porosity, and retention curves were deduced from the laboratory experiments mentioned in Section 2.2. We used three retention curves (Table 2, Figure 2). The first is the classical retention curve of van Genuchten (1980):

$$S_l = S_{l,r} + (S_{l,s} - S_{l,r}) \left[1 + \left(\frac{p_g - p_l}{p_e} \right)^{\frac{1}{1-m}} \right]^{-m} \quad (2)$$

where the air-entry pressure, p_e , depends on temperature through the surface tension.

$$p_e = p_{e,20} \frac{\sigma}{\sigma_{20}} \quad (3)$$

The second is a retention curve that has been extended with a branch for oven dryness. Instead of being constant, the residual saturation ($S_{l,r}$) is written, according to Rossi and Nimmo (1994), as

$$S_{l,r} = \alpha S_0 \ln \left(\frac{p_{dry}}{p_g - p_l} \right) \quad (4)$$

The third is composed of two porosities each with its own retention curve (Durner, 1994):

$$S_l = f_1 \left[1 + \left(\frac{p_g - p_l}{p_{e,1}} \right)^{\frac{1}{1-m_1}} \right]^{-m_1} + f_2 \left[1 + \left(\frac{p_g - p_l}{p_{e,2}} \right)^{\frac{1}{1-m_2}} \right]^{-m_2} \quad (5)$$

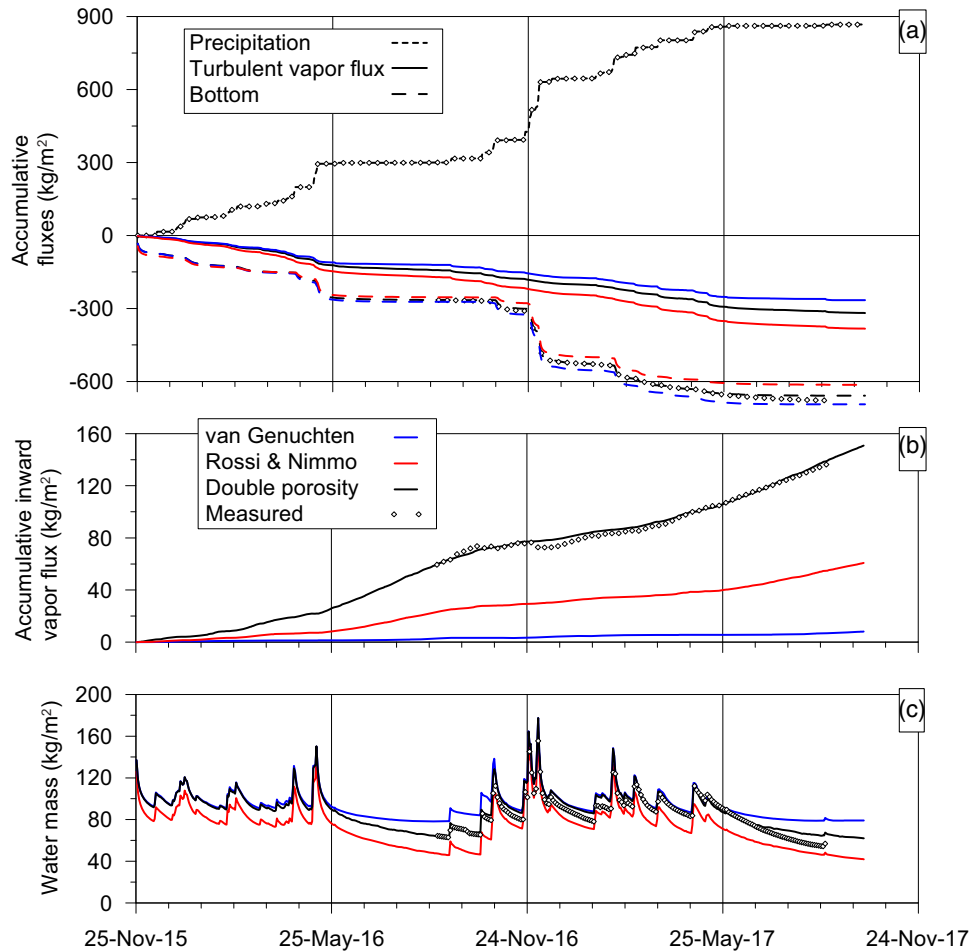


FIGURE 3 (a and b) Accumulative boundary fluxes and (c) mass of water in the lysimeter. Inflow is positive, and outflow is negative. Note that the measured and modeled rainwater is exactly the same, because measurements were used as input. In all graphs, blue, red, and black lines refer to the models of van Genuchten, Rossi and Nimmo, and double porosity, respectively

TABLE 3 Averaged boundary fluxes measured and of the three models between 1 Sept. 2016 and 31 Aug. 2017

Model	Rainfall	Bottom outflow	kg m ⁻² yr ⁻¹		
			Net vapor flux	Inward vapor flux	Outward vapor flux
Measured	567	-413	-163	77	-241
Double porosity	567	-395	-173	81	-254
Rossi and Nimmo	567	-360	-211	32	-242
van Genuchten	567	-420	-148	3	-150

where the two air-entry pressures ($p_{e,1}$ and $p_{e,2}$) depend on temperature the same way as in Equation 3. The three retention curves are almost identical for low suctions, but they differ for high suctions (Figure 2). The laboratory data of the various samples suggest differences between porosities (or maximum saturation, $S_{1,r}$) which may be due to heterogeneity but also to differences in the handling of the soil samples. Laboratory data also show variation for the higher suctions, where admittedly there are

also fewer data points. Nevertheless, the Rossi and Nimmo retention curve appears to resemble best the laboratory data.

Darcy's law for unsaturated flow of a phase α (either liquid or gas) is written as

$$\mathbf{q}_\alpha = -\frac{\mathbf{K}_{\text{int}} k_{r,\alpha}}{\mu_\alpha} (\nabla p_\alpha - \rho_\alpha \mathbf{g}) \quad (6)$$

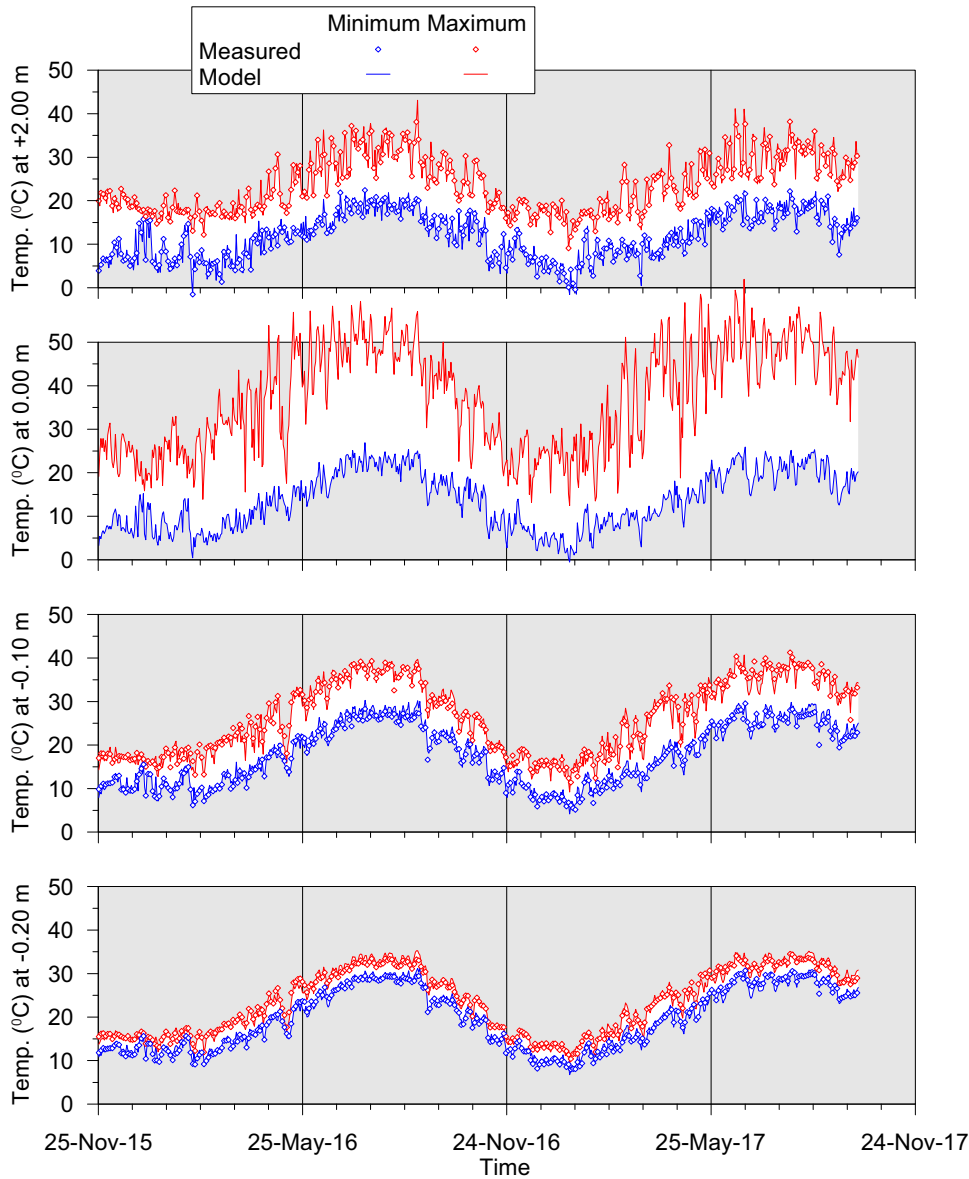


FIGURE 4 Daily minimum and maximum temperatures (temp.) for various depths up to 20 cm. Note that the measured and modeled temperature at +2 m is exactly the same, because measurements were used as input

The viscosity, μ_α , depends on temperature. The relative permeabilities ($k_{r,l}$ and $k_{r,g}$) are calculated according to

$$k_{r,l} = \sqrt{S_{l,e}} \left[1 - \left(1 - S_{l,e}^{1/m} \right)^m \right]^2 S_{l,e} = \frac{S_l - S_{l,r}^*}{S_{l,s} - S_{l,r}^*} \quad (7)$$

$$k_{r,g} = 1 \quad (8)$$

where residual saturation, $S_{l,r}^*$, equals $S_{l,r}$ when the van Genuchten retention curve is used (Equation 2), equals S_0 when a retention curve with oven dryness branch is used (Equation 4), and equals f_2 when a double porosity retention curve is used (Equation 7). The value for \mathbf{K}_{int} in Table 2 (which correspond to a saturated hydraulic conductivity of 10^{-4} m s^{-1}) is obtained from infiltration experiments and is a

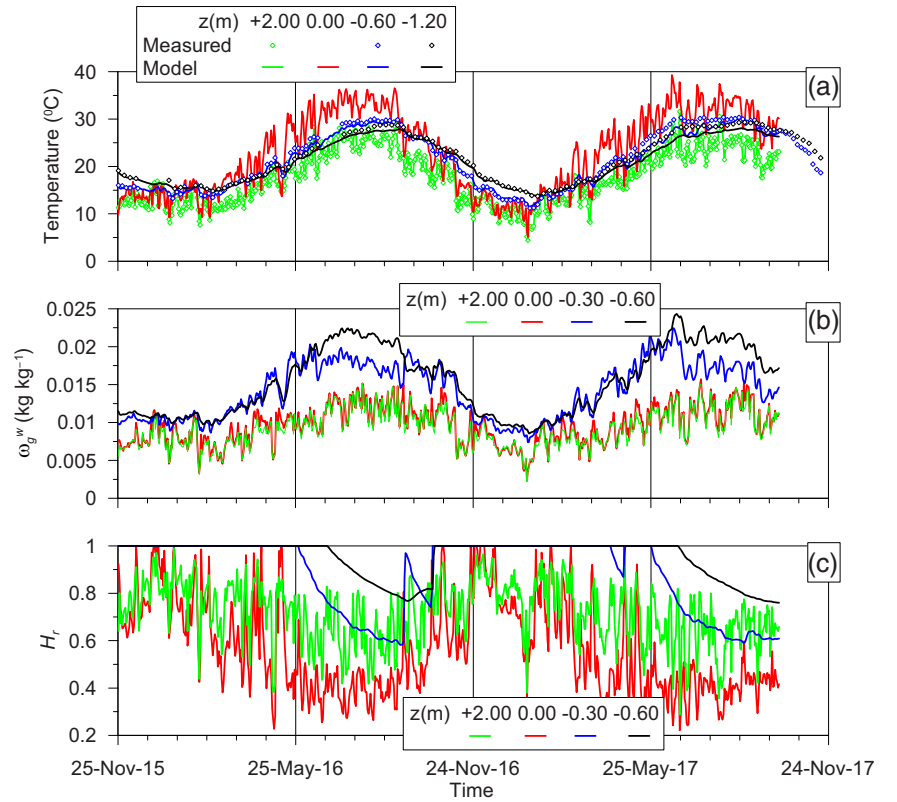
typical value for sand. Equation 7 can be extended further to cover dry conditions (Priesack & Durner, 2006; Zhang, 2011). However, such extensions hardly had an effect on the results, probably because in these dry conditions, the Darcy flux is negligible with respect to vapor diffusion, at least for sandy soils. For simplicity, we maintained Equation 7.

The vapor diffusion coefficient depends on temperature and gas pressure:

$$D_{dif,g}^w = \tau D_0 \frac{(273.15 + T)^n}{p_g} \quad (9)$$

The factor τ takes into account tortuosity and the enhancement of vapor diffusion due to phenomena taking place at the pore scale which cannot be modeled directly (Philip &

FIGURE 5 (a) Daily averaged temperatures, (b) specific humidity (ω_g^w), and (c) relative humidity (H_r) for various depths (z). Note that the measured and modeled temperature at +2 m is exactly the same, because measurements were used as input



de Vries, 1957). The parameters in Table 2 (D_0 , n , and τ) and a gas pressure of 10^3 hPa give a vapor diffusion coefficient of 1.4×10^{-4} and $2.1 \times 10^{-4} \text{ m}^2 \text{ s}^{-1}$ for 0 and 50°C , respectively.

The thermal conductivity depends on porosity and saturation:

$$\lambda = \lambda_{\text{sat}} \sqrt{S_l} + \lambda_{\text{dry}} (1 - \sqrt{S_l}) \quad (10)$$

$$\lambda_{\text{dry}} = \lambda_s^{(1-\phi)} \lambda_g^\phi \quad (11)$$

$$\lambda_{\text{sat}} = \lambda_s^{(1-\phi)} \lambda_l^\phi \quad (12)$$

The value for λ_s in Table 2 is obtained from calibration. The thermal conductivities of the other phases (λ_g and λ_l) are standard values. The parameters in Table 2 (ϕ , λ_g , λ_l , and λ_s) and Equations 11 and 12 give a thermal conductivity of $0.4 \text{ J } ^\circ\text{C}^{-1} \text{ m}^{-1} \text{ s}^{-1}$ when the soil is completely dry (λ_{dry}) and of $1.3 \text{ J } ^\circ\text{C}^{-1} \text{ m}^{-1} \text{ s}^{-1}$ when the soil is completely water-saturated (λ_{sat}). The average saturation degree of the dune sand is ~ 0.1 . This gives a thermal conductivity (λ) of $0.7 \text{ J } ^\circ\text{C}^{-1} \text{ m}^{-1} \text{ s}^{-1}$ according to Equation 10.

Specific humidity or vapor mass fraction is calculated by using the Kelvin equation (Edlefsen & Anderson, 1943):

$$\omega_g^w = \omega_{g,\text{sat}}^w H_r = \omega_{g,\text{sat}}^w \exp \left[\frac{(p_l - p_g) M^w}{R_g (273.15 + T) \rho_l} \right] \quad (13)$$

where the saturated specific humidity (or saturated vapor mass fraction, $\omega_{g,\text{sat}}^w$) is a function of temperature:

$$\omega_{g,\text{sat}}^w = \frac{1.36075 \times 10^{11} M^w}{R_g (273.15 + T) \rho_g} \exp \left(\frac{-5,239.7}{273.15 + T} \right) \quad (14)$$

The psychrometric chart of Figure 1 has been obtained from Equations 13 and 14. Note that the relative humidity, H_r , depends mainly on suction ($p_g - p_l$) and that the saturated specific humidity, $\omega_{g,\text{sat}}^w$, depends on temperature. A constant relative humidity in the psychrometric chart also implies a constant suction and, through the retention curve, a constant saturation. Moreover, the term for vapor diffusion in Equation A4, $\mathbf{j}_{\text{dif},g}^w$, can be written in terms of suction (or liquid pressure) gradient and temperature gradient as shown by Philip and de Vries (1957):

$$\begin{aligned} \mathbf{j}_{\text{dif},g}^w &= -\phi \rho_g S_g D_{\text{dif},g}^w \nabla \omega_g^w = \\ &= -\phi \rho_g S_g D_{\text{dif},g}^w \left(\omega_{g,\text{sat}}^w \frac{dH_r}{dp_l} \nabla p_l + H_r \frac{d\omega_{g,\text{sat}}^w}{dT} \nabla T \right) \end{aligned} \quad (15)$$

3.2 | Boundary and initial conditions

As our objective is to study the processes involved in water vapor adsorption, it is important to simulate the processes in

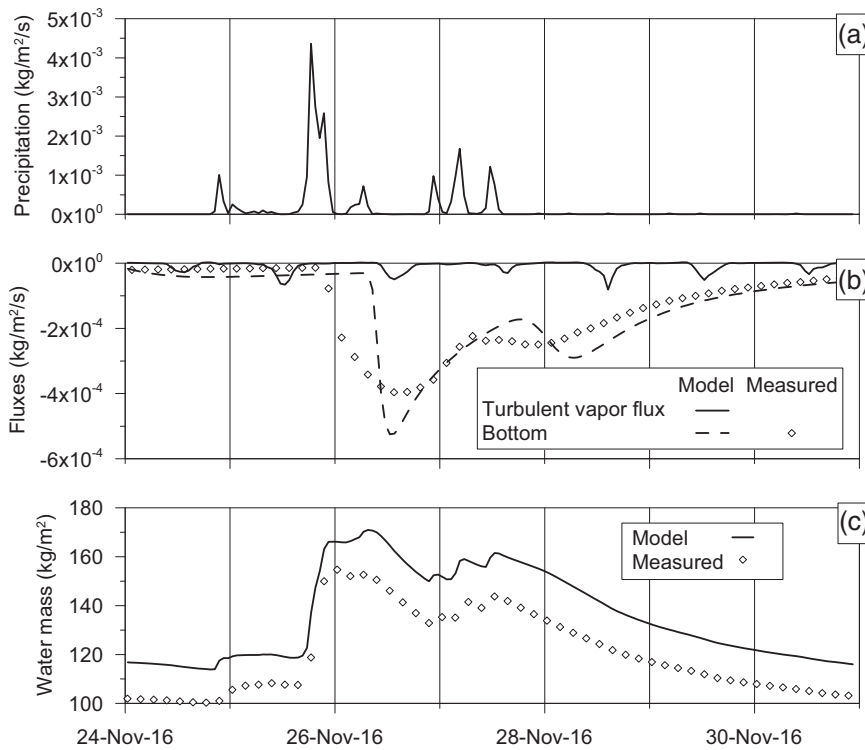


FIGURE 6 (a and b) Boundary fluxes and (c) mass of water in the lysimeter during a period of heavy rainfall. Inflow is positive, and outflow negative

their more fundamental form, especially the turbulent vapor fluxes at the soil surface. Therefore, we do not want to use the lysimeter data directly for a prescribed flow boundary condition, as was done, for instance, by Dijkema et al. (2018). Instead, we calculate these fluxes through a more fundamental relationship (Equation 17), and we use the lysimeter data for calibration.

In general, the top or atmospheric boundary of the model is used to represent the interaction between soil and atmosphere, including precipitation, evaporation, and solar radiation. As there is no vegetation, transpiration by plants is not considered. Also, mist deposition is neglected, because no correlation could be observed between measured water vapor adsorption and meteorological data (Kohfahl et al., 2019), including 100% relative humidity, required for mist formation. Fluxes of water, air, and energy are calculated as a function of meteorological measured data (rainfall, temperature, net radiation, relative humidity, and wind velocity) and the state variables (p_1 , p_g , and T) at the soil surface (to be calculated by the model). Hourly averaged meteorological data are used. Flux of water (j^w) at the boundary is specified as the sum of precipitation (P), turbulent vapor flux (E), and advective flux of vapor in the gas phase ($j_{g,adv}^w$):

$$j^w = P + E + j_{g,adv}^w \quad (16)$$

Turbulent vapor flux at the boundary (E) is strongly related to the phase change of water (evaporation or condensation) taking place within the soil, but it is not exactly the same in our conceptual model. The reason is that the amount of

vapor in the soil and its change are very small. Therefore, because of vapor mass balance, the turbulent vapor flux at the soil surface, E (in $\text{kg m}^{-2} \text{s}^{-1}$), must be (almost) equal to the condensation minus evaporation integrated over soil depth (also in $\text{kg m}^{-2} \text{s}^{-1}$). The latter, when it is positive (i.e., when condensation exceeds evaporation), can be equated to water vapor adsorption. The advective vapor flux across the soil surface ($j_{g,adv}^w$, see below) is generally very small and is neglected by many researchers (Saito et al., 2006), precipitation is measured, and the turbulent vapor flux is calculated by an aerodynamic relation (van Bavel & Hillel, 1976):

$$E = \frac{(\rho_g \omega_g^w)_{z_a} - (\rho_g \omega_g^w)_{z_0}}{r_a} \quad (17)$$

$$r_a = k^{-2} v_{z_a}^{-1} \left[\ln \left(\frac{z_a}{z_0} \right) \right]^2 \quad (18)$$

Vapor mass fraction in the air [$(\omega_g^w)_{z_a}$] can be calculated from measured relative humidity and temperature through Equations 13 and 14. Also, wind velocity at 2-m height (v_{z_a}) is measured. Vapor mass fraction at roughness length [$(\omega_g^w)_{z_0}$] is assumed to be equal to that at the soil surface and thus is a function of variables to be calculated by the model. Roughness length (z_0) is calibrated (see Table 2). The flux of energy (j^e) is specified as the sum of net radiation (R_n), sensible heat flux (H), latent heat flux (or advective heat flux due to vapor

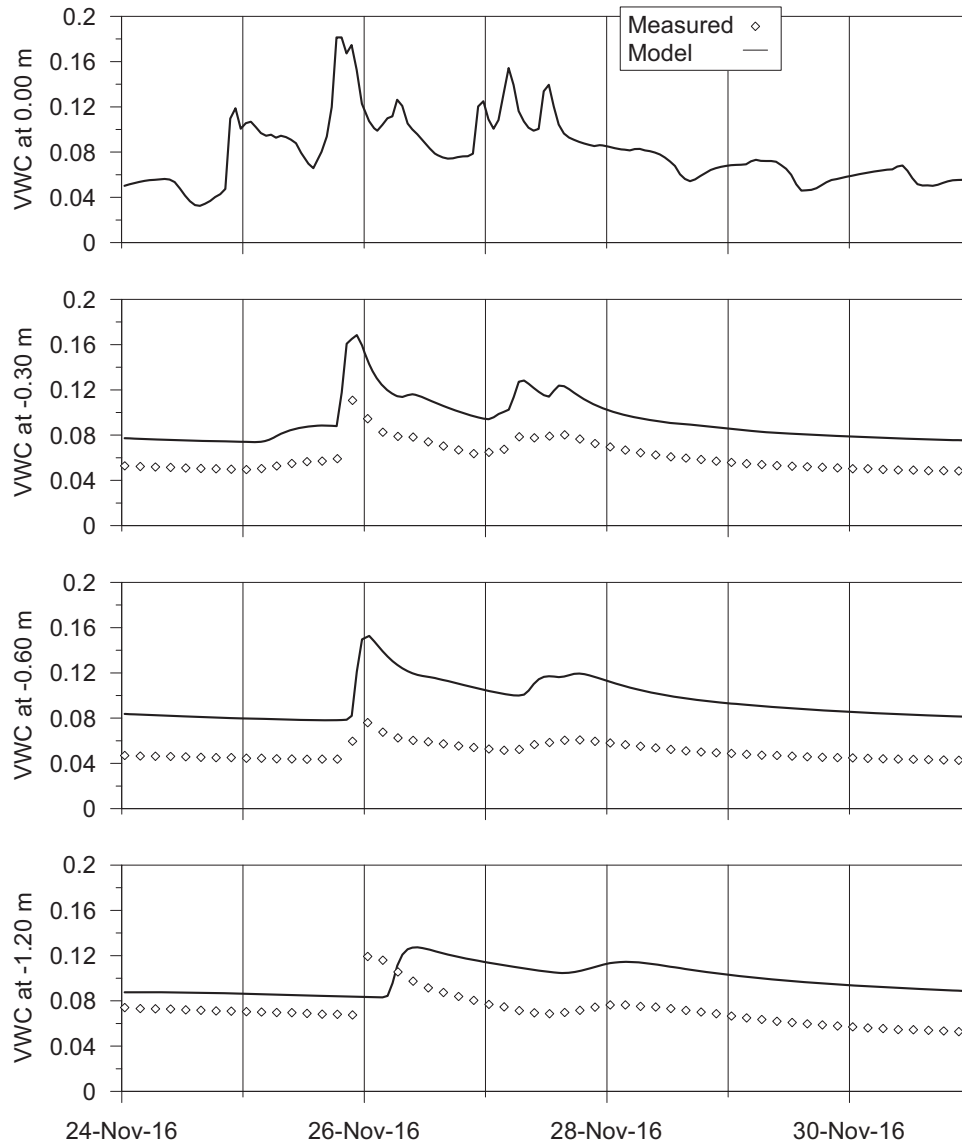


FIGURE 7 Volumetric water content (VWC) at various depths during a period of heavy rainfall

flux), and advective heat fluxes due to fluxes of liquid water and air.

$$j^c = R_n + H + (E + j_{g,adv}^w) e_g^w + P e_1^w + j_g^a e_g^a \quad (19)$$

The last two terms are generally very small and are most often neglected in other studies. Similar to vapor flux, the sensible heat flux (H) is calculated by an aerodynamic turbulent relation:

$$H = \rho_g c_g \frac{T_{za} - T_{z0}}{r_a} \quad (20)$$

where air temperature (T_{za}) is measured, and temperature at roughness length (T_{z0}) is assumed to be equal to that at the soil surface and thus is a variable to be calculated by the model. It is worth mentioning that Equations 16–20 use similar data

and assumptions as standard methods for calculating reference evaporation through the Penman–Monteith equation (Allen, Pereira, Raes, & Smith, 1998). The main difference is that Penman–Monteith assumes the soil surface to be saturated in water vapor (i.e., $H_r = 1$), whereas Equation 17 does not.

For the bottom of the model, we assumed gravitational flow, which is equivalent to a zero liquid pressure gradient ($\nabla p_l = 0$). According to Equation 6, this leads to a water flux that depends on capillary pressure through the relative permeability and retention curve. The temperature at the bottom was prescribed at measurements from the same location. For the air balance (Equation A2), the gas pressure is fixed to the atmospheric pressure of 0.1 MPa at the top boundary. From this, an air flow (j_g^a) and advective vapor flux ($j_{g,adv}^w$) can be calculated. A zero-air-flux boundary condition was used at the bottom.

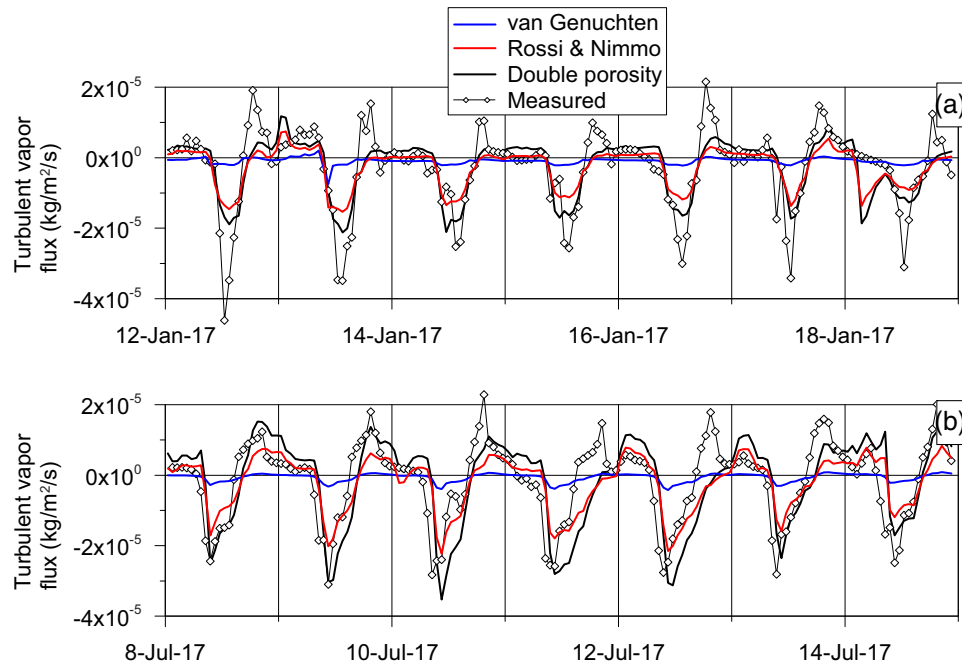


FIGURE 8 Evolution of turbulent vapor flux at the soil surface (E , Equation 17) during a week in (a) winter and (b) summer. Positive refers to inward fluxes, and negative refers to outward fluxes

Initial liquid pressure in the whole domain is 945 hPa (which corresponds to a suction of 55 hPa). This gives a uniform VWC that was more or less measured at various depths. Initial gas pressure is 1,000 hPa. Initial temperatures are calculated by linear interpolation of measured temperatures.

4 | RESULTS AND DISCUSSION

The model with the double porosity retention curve gave the best fit with the measurements. Therefore, we will first discuss the results of this model. Then, we will look at the differences compared with the models using the other retention curves.

4.1 | Accumulative water fluxes

On a yearly time scale, the model fits well the accumulative flux measured at the bottom (Figure 3a), the accumulative vapor influx (Figure 3b), and the mass of water (Figure 3c). This means that, because of water balance, on this time scale the model also reproduces well the average net turbulent flux at the boundary (related to condensation–evaporation). The measured mass of water was deduced by subtracting the mass of solid in the lysimeter from the total weight of the lysimeter. The mass of solid is calculated from porosity and density of the solid. This means that, for instance, an error in the porosity of $0.01 \text{ m}^3 \text{ m}^{-3}$ gives an error in mass of water of 40 kg (0.01 times volume of lysimeter times density of the solid). As porosity is not supposed to change in time,

this error should be systematic and not effect changes in mass of water. Therefore, we should focus on the changes in mass rather than the absolute values. Table 3 shows simulated inward turbulent vapor flux at the boundary of 1 yr (related to water vapor adsorption) and measurements of vapor adsorption calculated by Equation 1. Simulated inward turbulent vapor flux (or water vapor adsorption) is $81 \text{ kg m}^{-2} \text{ yr}^{-1}$ ($0.22 \text{ kg m}^{-2} \text{ d}^{-1}$), which is comparable with the values obtained by Agam and Berliner (2004), Kosmas et al. (2001), Uclés et al. (2015), and Dijkema et al. (2018), Verhoef et al. (2006), mentioned in the introduction.

4.2 | Temperature and humidity oscillations

The model fits the temperatures well (Figures 4 and 5). This could be done by calibrating the roughness length (z_0), which controls the amplitude of temperature oscillations, and the thermal conductivity of the solid (λ_s), which controls the downward damping of this amplitude (Table 3). Some typical natural phenomena can be observed. The daily oscillations are largest at the soil surface (larger than in the air at 2 m, Figure 4). This reflects the fact that solar radiation first heats the soil surface, which in turn heats the atmosphere and underlying soil (Jury & Horton, 2004). Also, the daily averaged temperatures at the soil surface are higher than air temperatures, especially during summer (Figure 5). The surface adsorbs more solar radiation than the atmosphere, which is compensated through sensible and latent heat fluxes that require a temperature difference between soil surface and air.

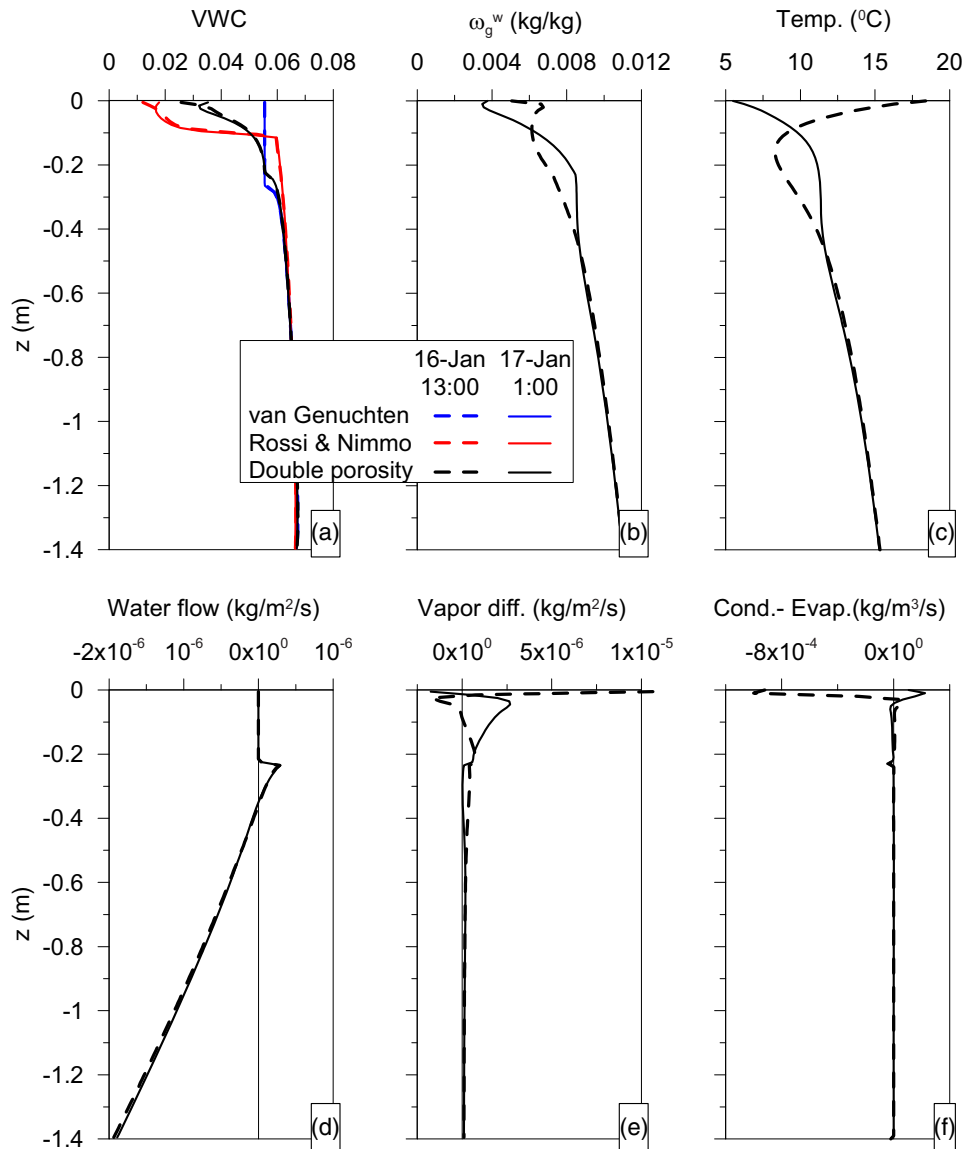


FIGURE 9 Profiles during winter of (a) volumetric water content (VWC), (b) vapor mass fraction (ω_g^w), (c) temperature (temp.), (d) fluxes of liquid water flow, (e) vapor diffusion (diff.), and (f) condensation–evaporation (cond.–evap.) of water. Positive fluxes are upward, negative fluxes are downward. Condensation is positive, and evaporation is negative. The y axis shows depth (z)

Daily fluctuations are damped at depths of, at most, a few decimeters (Figure 4). Yearly oscillations are damped at much larger depths (Figure 5).

The specific humidity (or vapor mass fraction, ω_g^w) at the soil surface together with that of the air does not show a lot of variation, in contrast with the specific humidity at larger depths where the soil gas is clearly more humid during the summer. The opposite occurs for the relative humidity (Figure 5). The reason is that at larger depths the liquid saturation (S_l), and therefore suction ($p_g - p_l$) and relative humidity (H_r), remain more constant. However, the high temperatures in summer cause an increase in saturated vapor mass fraction according to Equation 14. A roughly constant relative humidity together with a high saturated vapor mass

fraction ($\omega_{g,sat}^w$) implies an also high vapor mass fraction (ω_g^w) according to Equation 13. In other words, in the psychrometric chart of Figure 1, one is moving along a line of equal relative humidity. On the other hand, the soil surface desiccates more quickly, adopting a humidity closer to that of the air, with a more horizontal movement in the psychrometric chart.

4.3 | Heavy rainfall event

Figures 6 and 7 show the results of the model and measurements for a week with heavy rainfall. The model reproduces the general effect of the rainfall, but it overestimates the total amount of water in the lysimeter and the VWC. Moreover, flux

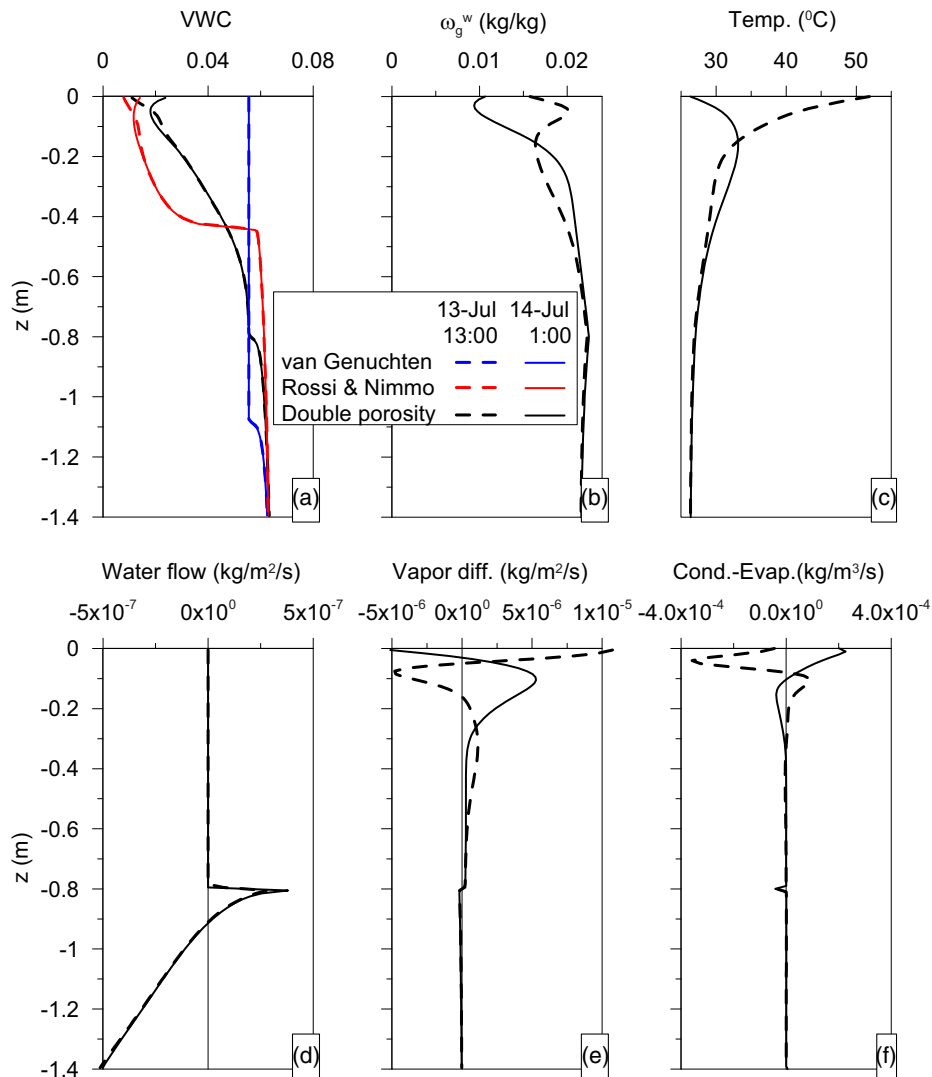


FIGURE 10 Profiles during summer of (a) volumetric water content (VWC), (b) vapor mass fraction (ω_g^w), (c) temperature (temp.), (d) fluxes of liquid water flow, (e) vapor diffusion (diff.), and (f) condensation–evaporation (cond.–evap.) of water. Positive fluxes are upward, negative fluxes are downward. Condensation is positive, and evaporation is negative. The y axis shows depth (z)

data indicate that the model simulates less attenuation of the rainfall events than the measurements. Maybe the fit can be improved by calibrating the intrinsic permeability and parameters for the relative permeability curve. However, since VWC is mostly low, it is not supposed to have a relevant impact on other processes, such as heat flow and evaporation, which is the focus of this work.

4.4 | Analysis of a week in summer and in winter

Figure 8 shows the vapor fluxes at the boundary during a week in summer and in winter. During the day, there is clearly a negative (or outward) turbulent vapor flux, related to evaporation. At night, this is reversed. The model results show similar oscillations as the measurements. Nevertheless,

during summer, the modeled oscillations are somewhat delayed with respect to the measurements. The reason is not clear, but it may be related to hysteresis of the retention curve, not considered by our models. The large measured inward turbulent vapor flux during the afternoon is not reproduced by the model. Also, the model underestimates the size of the oscillations in turbulent vapor flux during the winter.

To gain insight into the dynamics of the processes taking place, we have plotted profiles of various variables for a point of time at night and at day in winter (Figure 9) and in summer (Figure 10). For both winter and summer, we can observe an evaporation front at about 0.2 and 0.8 m, respectively, similar to what was found by Gran, Carrera, Massana, et al. (2011) and Gran, Carrera, Olivella, and Saaltink (2011). Deep below this front, water flows downwards, enabling the drainage at the lower boundary. Up to 0.1 m below the front, liquid water flows upwards, evaporates at the front, and continues

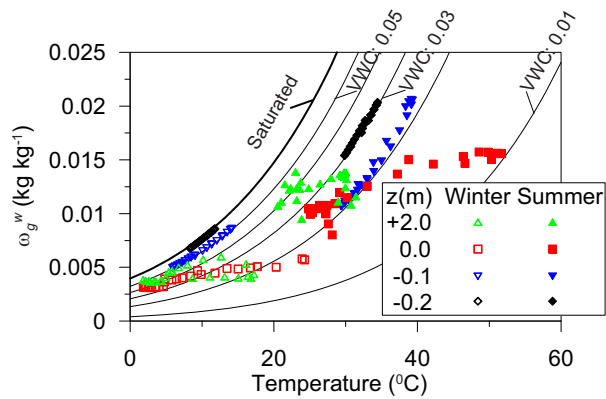


FIGURE 11 Psychrometric chart with results of the model during a day in winter (16 Jan. 2017) and in summer (13 July 2017). It also contains lines of equal volumetric water content (VWC) for the double porosity retention curve. The y axis shows specific humidity (ω_g^w), and depth (z) is indicated by symbol color

its upward transport as vapor diffusion. Note that just below the evaporation front (0.2 m in winter and 0.8 m in summer), there is a little bit of vapor diffusion that is upwards in winter and downwards in summer, caused by the downward and upward gradient of humidity (ω_g^w), respectively. This in turn is caused by the downward and upward gradient of temperature. Above the evaporation front flow of liquid water is practically zero and water is mainly transported by vapor diffusion, called by Or, Lehmann, Shahraeeni, and Shokri (2013) a Stage II evaporation. Specific humidity (ω_g^w) near the surface is very close to that of the air at +2 m and oscillates only slightly in comparison with the temperature. We can see more clearly the effect of the large temperature oscillations and relatively stable specific humidity, if we plot the results in a psychrometric chart (Figure 11). Instead of lines of equal relative humidity, Figure 11 contains lines of equal VWC, which can be calculated from Kelvin's law (Equation 13), temperature dependency of saturated humidity (Equation 14), and the retention curve (Equation 5). Near the surface, the large temperature oscillations cause oscillations in relative humidity and thus trigger the changes in VWC. The water for this VWC change is taken from or released to the atmosphere as vapor. On the other hand, at slightly deeper levels (−0.2 m in summer, −0.1 m in winter) the VWC hardly changes. Beside temperature oscillations, Figure 11 also illustrates the importance of the retention curve, as a different retention curve can give utterly different values for the lines of equal VWC. The changing temperatures and VWCs create an intricate dynamic pattern of bands of upward or downward diffusion and condensation or evaporation. As the gradient of specific humidity ($\nabla\omega_g^w$) changes drastically with depth, vapor diffusion, being proportional to $\nabla\omega_g^w$ (Equation 15), changes accordingly. Note that in Figures 9 and 10, the peaks and troughs of the specific humidity profiles coincide with a zero vapor diffusion and that the peaks and troughs of the vapor

diffusion profiles coincide with zero condensation–evaporation. This can be explained by considering a simple steady-state mass balance for water vapor in which diffusion is the only transport process. In that case, condensation–evaporation equals the divergence of the vapor diffusion ($\nabla\mathbf{j}_{\text{dif},g}^w$).

4.5 | Effect of retention curve

Using different retention curves of Table 2 and Figure 2 has some effect on the yearly net turbulent vapor flux at the top boundary (Table 3 and Figure 6). More importantly, the retention curve has a very big effect on the modeled daily oscillation of the turbulent vapor flux (Figure 8). Oscillations are significantly reduced for the Rossi and Nimmo retention curve and practically disappear for the van Genuchten retention curve. As a consequence, the average inward turbulent vapor flux is also reduced a lot (Figure 3, Table 3). The reason is that the van Genuchten retention curve that we used gives a constant VWC for suctions higher than $\sim 10^3$ hPa (see Figure 2), which corresponds to a practically saturated relative humidity (~ 0.9993). This means that in a psychrometric chart, such as Figure 11, changes in temperature and specific humidity will not result in any changes of VWC unless very close to the saturation line. For the Rossi and Nimmo retention curve, there are changes of VWC, but less than for the double porosity retention curve. The same can be seen in Figure 10. In summer, the model of the van Genuchten retention curve shows that the VWC of the upper part is at its constant residual value both at night and noon. The model of the Rossi and Nimmo retention curve shows some difference between night and noon, but not as much as the model of the double porosity. In any case, the model with the double porosity better reproduces the observed oscillations, although the Rossi and Nimmo model agrees better with the measured retention curve (Figure 2).

5 | SUMMARY AND CONCLUSIONS

A numerical model taking into account water, vapor, and heat transport in unsaturated soil could simulate the water adsorption deduced from the daily oscillations of the mass of water, measured in the lysimeter. Simulated and measured water vapor adsorption is 81 and 77 kg m^{−2} yr^{−1}, respectively (inward vapor flux in Table 3), which is comparable with other studies.

The model shows that water vapor adsorption is driven by daily temperature oscillations at the soil surface, which can be much higher than oscillations in air temperature (typically measured at a height of 2 m). On the other hand, specific (or absolute) humidity remains more constant. This means

that relative humidity and suction will oscillate according to Kelvin's law (Equation 13) and the temperature dependency of saturated humidity (Equation 14). In turn, according to the retention curve, this leads to oscillation in retained water. This is illustrated in Figure 11, showing that large oscillation in temperature with constant specific humidity must lead to large changes in relative humidity and, depending on the retention curve, in VWC. The required water is taken from or released to the atmosphere through vapor flux across the soil surface, represented by E in Equation 17, followed by condensation–evaporation within the soil. Both experimental and model results demonstrate that this vapor flux can oscillate significantly during a day. Water vapor adsorption can be understood best as an inward or negative vapor flux.

The retention curve, particularly its driest part, plays an important role in this mechanism. It determines the amplitude of the oscillations of vapor flux across the soil surface. When for high suctions in the retention curve the VWC changes more with suction, this flux also oscillates more. Therefore, a retention curve of van Genuchten with a constant residual saturation hardly gives any oscillation. A double porosity retention curve gives the highest oscillations similar to the measurements. Nevertheless, one can question the correctness of this retention curve. It suggests a 15% (f_2 in Table 2) content of fine material such as clay, but measured grain size distributions give clay contents between 0.3 and 3.1%. It is probable that other factors are involved that have not been considered by the model, such as hysteresis of the retention curve and/or heterogeneity in the soil. Although the macroscopic appearance and the sediment analyses of the dune sands revealed a homogeneity at the lysimeter scale, local heterogeneities may occur due to internal layering of the dune sediments not considered in the model. Studies at the pore scale have revealed that condensation–evaporation can be slow to reach equilibrium, taking up to hours for high vapor saturation (Shahraeeni & Or, 2010). Therefore, with daily oscillations of temperature and relative humidity, condensation–evaporation may become kinetically controlled, whereas our models assume a macroscopic equilibrium between suction, relative humidity, temperature, and VWC. Anyhow, our results suggest that in order to study water vapor adsorption well, it is important to characterize the driest part of the retention curve adequately.

According to the double porosity model, water vapor adsorption affects the top few decimeters of the soil, where daily temperature oscillations are substantial. The condensation–evaporation in the soil profile is far from uniform. The model suggests a pattern of alternating bands of condensation and evaporation. It is difficult to measure these small scale patterns directly with current techniques such as lysimeters, sensors in soils, and meteorological data. More information on this can be obtained from numerical models that are calibrated to changes in mass of water in precision weighing meteo-lysimeters.


ACKNOWLEDGMENTS

We are very grateful to André Peters for providing the AWAT filter and give special thanks to Daniel Jesus Martínez, Fernando Ruiz Bermudo, and Antonio Nicolas Martínez for their excellent technical assistance and support. We are grateful for the support and collaboration of the Biological Station of Doñana, the Biological Reserve of Doñana, and the administration of the Doñana National Park. The contract of Lidia Molano Leno (PEJ-2014-A-68763) was financed by the Ministry of Economy, Industry and Competitiveness of Spain (MINECO) and co-financed by the European Investment Bank (EIB) and the European Social Fund (ESF). Likewise, this work has been financed by the CLIGRO Project (MICINN, CGL2016-77473-C3-1-R) of the Spanish National Plan for Scientific and Technical Research and Innovation. The infrastructure has been co-financed by European Research Funds (SE Scientific Infrastructures and Techniques and Equipment 2013, IGME13-1E-2113).

CONFLICT OF INTEREST

The authors declare no conflict of interest.

ORCID

Maarten W. Saaltink 

<https://orcid.org/0000-0003-0553-4573>

REFERENCES

- Agam, N., & Berliner, P. R. (2004). Diurnal water content changes in the bare soil of a coastal desert. *Journal of Hydrometeorology*, 5, 922–933. [https://doi.org/10.1175/1525-7541\(2004\)005%3C0922:DWCCIT%3E2.0.CO;2](https://doi.org/10.1175/1525-7541(2004)005%3C0922:DWCCIT%3E2.0.CO;2)
- Agam, N., & Berliner, P. R. (2006). Dew formation and water vapor adsorption in semi-arid environments: A review. *Journal of Arid Environments*, 65, 572–590. <https://doi.org/10.1016/j.jaridenv.2005.09.004>
- Allen, R. G., Pereira, L. S., Raes, D., & Smith, M. (1998). *Crop evapotranspiration: Guidelines for computing crop water requirements* (FAO Irrigation and Drainage Paper 56). Rome: FAO.
- Carrier, W. H. (1911). Rational psychrometric formulae: Their relation to the problems of meteorology and of air conditioning. *Journal of the American Society of Mechanical Engineers*, 33, 1309–1345.
- Dijkema, J., Koonce, J. E., Shillito, R. M., Ghezzehei, T. A., Berli, M., van der Ploeg, M. J., & van Genuchten, M. Th. (2018). Water distribution in an arid zone soil: Numerical analysis of data from a large weighing lysimeter. *Vadose Zone Journal*, 17(1). <https://doi.org/10.2136/vzj2017.01.0035>
- Durner, W. (1994). Hydraulic conductivity estimation for soils with heterogeneous pore structure. *Water Resources Research*, 30, 211–223. <https://doi.org/10.1029/93WR02676>
- Edlefsen, N. E., & Anderson, A. B. C. (1943). Thermodynamics of soil moisture. *Hilgardia*, 15, 31–298. <https://doi.org/10.3733/hilg.v15n02p031>
- Gran, M., Carrera, J., Massana, J., Saaltink, M. W., Olivella, S., Ayora, A., & Lloret, A. (2011). Dynamics of water vapor flux and water separation processes during evaporation from a salty dry

- soil. *Journal of Hydrology*, 396, 215–220. <https://doi.org/10.1016/j.jhydrol.2010.11.011>
- Gran, M., Carrera, J., Olivella, S., & Saaltink, M. W. (2011). Modeling evaporation processes in a saline soil from saturation to oven dry conditions. *Hydrology and Earth System Sciences*, 15, 2077–2089. <https://doi.org/10.5194/hess-15-2077-2011>
- Grifoll, J., Gastó, J. M., & Cohen, Y. (2005). Non-isothermal soil water transport and evaporation. *Advances in Water Resources*, 28, 1254–1266. <https://doi.org/10.1016/j.advwatres.2005.04.008>
- Grifoll, J. (2013). Contribution of mechanical dispersion of vapor to soil evaporation. *Water Resources Research*, 49, 1099–1106. <https://doi.org/10.1002/wrcr.20105>
- Hannes, M., Wollschläger, U., Schrader, F., Durner, W., Gebler, S., Pütz, T., ... Vogel, H.-J. (2015). A comprehensive filtering scheme for high-resolution estimation of the water balance components from high-precision lysimeters. *Hydrology and Earth System Sciences*, 19, 3405–3418. <https://doi.org/10.5194/hess-19-3405-2015>
- Hatt, B., & Le Costumer, S. (2008). *Practice Note 1 in situ measurement of hydraulic conductivity facility for advancing water biofiltration*. Melbourne, VIC, Australia: Monash University.
- Hoffmann, M., Schwartengraber, R., Wessolek, G., & Peters, A. (2016). Comparison of simple rain gauge measurements with precision lysimeter data. *Atmospheric Research*, 174–175, 120–123. <https://doi.org/10.1016/j.atmosres.2016.01.016>
- Jiang, J., Zhao, L., & Zhai, Z. (2016). Estimating the effect of shallow groundwater on diurnal heat transport in a vadose zone. *Frontiers of Earth Science*, 10, 513–526. <https://doi.org/10.1007/s11707-015-0524-5>
- Jury, W. A., & Horton, R. (2004). *Soil physics* (6th ed.). Hoboken, NJ: Wiley & Sons.
- Kohfahl, C., Molano-Leno, L., Martínez, G., Vanderlinden, K., Guardiola-Albert, C., & Moreno, L. (2019). Determining groundwater recharge and vapor flow in dune sediments using a weighable precision meteorology lysimeter. *Science of the Total Environment*, 656, 550–557. <https://doi.org/10.1016/j.scitotenv.2018.11.415>
- Kosmas, C., Marathianou, M., Gerontidis, St., Detsis, V., Tsara, M., & Poesen, J. (2001). Parameters affecting water vapor adsorption by the soil under semi-arid climatic conditions. *Agricultural Water Management*, 48, 61–78. [https://doi.org/10.1016/s0378-3774\(00\)00113-x](https://doi.org/10.1016/s0378-3774(00)00113-x)
- Milly, P. C. D. (1982). Moisture and heat transport in hysteretic, inhomogeneous porous media: A matric head-based formulation and a numerical model. *Water Resources Research*, 18, 489–498. <https://doi.org/10.1029/WR018i003p00489>
- Olivella, S., Carrera, J., Gens, A., & Alonso, E. E. (1994). Nonisothermal multiphase flow of brine and gas through saline media. *Transport in Porous Media*, 15, 271–293. <https://doi.org/10.1007/BF00613282>
- Olivella, S., Gens, A., Carrera, J., & Alonso, E. E. (1996). Numerical formulation for a simulator (CODE_BRIGHT) for the coupled analysis of saline media. *Engineering Computations*, 13, 87–112. <https://doi.org/10.1108/02644409610151575>
- Or, D., Lehmann, P., Shahraeeni, E., & Shokri, N. (2013). Advances in soil evaporation physics: A review. *Vadose Zone Journal*, 12(4). <https://doi.org/10.2136/vzj2012.0163>
- Peters, A., Nehls, T., Schonsky, H., & Wessolek, G. (2014). Separating precipitation and evapotranspiration from noise: A new filter routine for high-resolution lysimeter data. *Hydrology and Earth System Sciences*, 18, 1189–1198. <https://doi.org/10.5194/hess-18-1189-2014>
- Philip, J. R., & de Vries, D. A. (1957). Moisture movement in porous materials under temperature gradients. *Eos*, 38, 222–232. <https://doi.org/10.1029/tr038i002p00222>
- Priesack, E., & Durner, W. (2006). Closed-form expression for the multimodal unsaturated conductivity function. *Vadose Zone Journal*, 5, 121–124. <https://doi.org/10.2136/vzj2005.0066>
- Pütz, T., Fank, J., & Flury, M. (2018). Lysimeters in vadose zone research. *Vadose Zone Journal*, 17(1). <https://doi.org/10.2136/vzj2018.02.0035>
- Rossi, C., & Nimmo, J. R. (1994). Modeling of soil water retention from saturation to oven dryness. *Water Resources Research*, 30, 701–708. <https://doi.org/10.1029/93WR03238>
- Saito, H., Šimůnek, J., & Mohanty, B. P. (2006). Numerical analysis of coupled water, vapor, and heat transport in the vadose zone. *Vadose Zone Journal*, 5, 784–800. <https://doi.org/10.2136/vzj2006.0007>
- Schrader, F., Durner, W., Fank, J., Gebler, S., & Pütz, T. (2013). Estimating precipitation and real evapotranspiration from precision lysimeter measurements. *Procedia Environmental Science*, 19, 543–552. <https://doi.org/10.1016/j.proenv.2013.06.061>
- Shahraeeni, E., & Or, D. (2010). Pore-scale analysis of evaporation and condensation dynamics in porous media. *Langmuir*, 26, 13924–13936. <https://doi.org/10.1021/la101596y>
- Tomaszkiewicz, M., Abou Najm, M., Beysens, D., Alameddine, I., & El-Fadel, M. (2015). Dew as a sustainable non-conventional water resource: A critical review. *Environmental Reviews*, 23, 425–442. <https://doi.org/10.1139/er-2015-0035>
- Uclés, O., Villagarcía, L., Cantón, Y., Lázaro, R., & Domingo, F. (2015). Non-rainfall water inputs are controlled by aspect in a semiarid ecosystem. *Journal of Arid Environments*, 113, 43–50. <https://doi.org/10.1016/j.jaridenv.2014.09.009>
- van Bavel, C. H. M., & Hillel, D. I. (1976). Calculating potential and actual evaporation from a bare soil surface by simulation of concurrent flow of water and heat. *Agricultural Meteorology*, 17, 453–476. [https://doi.org/10.1016/0002-1571\(76\)90022-4](https://doi.org/10.1016/0002-1571(76)90022-4)
- van Genuchten, M. Th. (1980). A closed-form equation for predicting the hydraulic conductivity of unsaturated soils. *Soil Science Society of America Journal*, 44, 892–898. <https://doi.org/10.2136/sssaj1980.03615995004400050002x>
- Verhoef, A., Díaz-Espejo, A., Knight, J. R., Villagarcía, L., & Fernández, J. E. (2006). Adsorption of water vapor by bare soil in an olive grove in southern Spain. *Journal of Hydrometeorology*, 7, 1011–1027. <https://doi.org/10.1175/JHM556.1>
- Zeng, Y., Wan, L., Su, Z., Saito, H., Huang, K., & Wang, X. (2009). Diurnal soil water dynamics in the shallow vadose zone (field site of China University of Geosciences, China). *Environmental Geology*, 58, 11–23. <https://doi.org/10.1007/s00254-008-1485-8>
- Zhang, Z. F. (2011). Soil water retention and relative permeability for conditions from oven-dry to full saturation. *Vadose Zone Journal*, 10, 1299–1308. <https://doi.org/10.2136/vzj2011.0019>

SUPPORTING INFORMATION

Additional supporting information may be found online in the Supporting Information section at the end of the article.

How to cite this article: Saaltink MW, Kohfahl C, Molano-Leno L. Analysis of water vapor adsorption in soils by means of a lysimeter and numerical modeling. *Vadose Zone J.* 2020;19:e220012. <https://doi.org/10.1002/vzj2.20012>

APPENDIX

BALANCE EQUATIONS

Balance equations are solved for water, air, and energy in an unsaturated medium. Both water and dry air (basically consisting of N_2 and O_2) can exist in the liquid and gas phase and be transported in these two phases through advection, diffusion, and dispersion. This can be expressed by the following balance equations:

$$\frac{\partial}{\partial t} \left(\phi S_l \rho_l \omega_l^w + \phi S_g \rho_g \omega_g^w \right) + \nabla \cdot \left(\mathbf{j}_l^w + \mathbf{j}_g^w \right) = f^w \quad (A1)$$

$$\frac{\partial}{\partial t} \left(\phi S_l \rho_l \omega_l^a + \phi S_g \rho_g \omega_g^a \right) + \nabla \cdot \left(\mathbf{j}_l^a + \mathbf{j}_g^a \right) = f^a \quad (A2)$$

$$\begin{aligned} & \frac{\partial}{\partial t} \left[e_s \rho_s (1 - \phi) + (e_l^w \omega_l^w + e_l^a \omega_l^a) \rho_l S_l \phi \right. \\ & \left. + (e_g^w \omega_g^w + e_g^a \omega_g^a) \rho_g S_g \phi \right] - \nabla \cdot (\lambda \nabla T) \\ & + \nabla \cdot \left(e_l^w \mathbf{j}_l^w + e_g^w \mathbf{j}_g^w + e_l^a \mathbf{j}_l^a + e_g^a \mathbf{j}_g^a \right) = f^e \quad (A3) \end{aligned}$$

where fluxes, \mathbf{j} , are composed of advective, diffusive and dispersive fluxes:

$$\mathbf{j}_\alpha^i = \rho_\alpha \omega_\alpha^i \mathbf{q}_\alpha - \phi \rho_\alpha S_\alpha D_{\text{dif},\alpha}^i \nabla \omega_\alpha^i - \phi \rho_\alpha S_\alpha \mathbf{D}_{\text{dis},\alpha}^i \nabla \omega_\alpha^i \quad (A4)$$

Note that we explicitly take into account gas flow, vapor advection, and dispersion like Grifoll et al. (2005), but unlike Milly (1982) and Saito et al. (2006), who neglect it. We added these fluxes for reasons of coherence in the mass balance equations. However, we do not expect them to have a lot of effect.

Internal energies, e_α^i in Equation A3, depend linearly on temperature:

$$\begin{aligned} e_l^w &= 4.184T \\ e_g^w &= 2.5 \times 10^6 + 1,900T \\ e_s &= 760T \\ e_l^a &= 1,000T \\ e_g^a &= 1,000T \end{aligned} \quad (A5)$$

where e_α^i is in joules per kilogram and T is in degrees Celsius. An important property is the latent heat of evaporation, which is represented by the difference between the internal energy of vapor and liquid water ($e_l^w - e_g^w = 2.5 \times 10^6 - 2,284T$), which in our approach depends slightly on temperature.